Strategy for refinement of nodal densities and integration cells in EFG technique

Bhavana S.S. Patel[*1,2], Babu K.S. Narayan[3a] and Katta Venkataramana[3a]

[1]*National Institute of Technology Karnataka, India*
[2]*RV College of Engineering, India*
[3]*National Institute of Technology Karnataka, India*

Abstract. MeshFree methods have become popular owing to the ease with which high stress gradients can be identified and node density distribution can be reformulated to accomplish faster convergence. This paper presents a strategy for nodal density refinement with strain energy as basis in Element-Free Galerkin MeshFree technique. Two popular flat plate problems are considered for the demonstration of the proposed strategies. Issue of integration errors introduced during nodal density refinement have been addressed by suggesting integration cell refinement. High stress effects around two symmetrical semi-circular notches under in-plane axial load have been addressed in the first problem. The second considers crack propagation under mode I and mode II fracture loading by the way of introducing high stress intensity through line crack. The computational efficacy of the adaptive refinement strategies proposed has been highlighted.

Keywords: adaptive refinement; element-free Galerkin; crack propagation; stress intensity; stress concentration

1. Introduction

Modelling components with difficult geometries, boundary conditions, discontinuities within the element, high stress gradients and automated re-meshing are still a challenge in numerical methods. Of all these difficulties, modelling crack propagation is one such issue which has attracted researchers all over the world. A crack cannot be initiated numerically, and therefore is pre-initiated and then its propagation path is simulated.

Finite Element Method (FEM) has the difficulty in automating the meshes at each step, as it needs to satisfy pre-defined mesh quality, which in turn requires human intervention. In FEM, the modelling of singular crack tip by introducing additional degrees-of-freedom (Mergheim *et al.* 2005) and modeling its propagation based on Stress Intensity Factor (SIF), computed using Virtual Crack Closure Technique (Chow and Atluri 1995, VCCT), strain energy release rate (Bouchard *et al.* 2003) have been attempted. Notwithstanding, FEM tends to follows the element edge for propagation of crack making the trace a zigzag path. Extended FEM (XFEM) has been introduced

---

∗Corresponding author, Assistant Professor, E-mail: bhavana8patel@gmail.com
[a]Professor

where the finite elements have been enriched with discontinuous functions to model cracks within the element and thereby reducing re-meshing. Here the enrichment and smoothing functions are used to model the crack tip and its path (Belytschko and Black 1999, Dolbow *et al*. 2000, Sukumar *et al*. 2000). Further, in ABAQUS® software, implementation of Heaviside function (Giner *et al*. 2009), and problems dealing with jumps, kink cracks, singularities are solved using XFEM (Sukumar and Belytschko 2000, Menouillard and Belytschko 2010). But, even with this added feature of element discontinuity, XFEM has limitations in modelling high stress gradients that occur during crack propagation. A number of MeshFree methods have been developed to address this issue; Element Free Galerkin (EFG) is one such method where with enrichment of the displacement field, crack can be modeled for 2D (Belytschko *et al*. 1995, Fleming 1997) and 3D (Krysl and Belytschko 1999) problems. The jump in the displacement field has been used to represent the crack, which is defined by discontinuous function and the closing of the crack tip by crack front function (Rabczuk *et al*. 2007, Zi *et al*. 2007, Rabczuk and Zi 2007). The use of Extended MeshFree method based on partition of unity for cohesive crack has been presented by Bordas *et al*. (2008), Pant *et al*. (2013).

Coupling MeshFree Method with XFEM (Eigel *et al*. 2010), MeshFree method with FEM (Wu *et al*. 2012), and buck*et al*gorithms (Liu and Tu 2002) have been attempted to enhance computationally efficiency. Refinement regions definition based on stress gradients (Haussler and Korn 1998) or recovery based methods (Ullah and Augarde 2013) have been suggested. Scheme for node placement using background triangular cells (Liu 2009) or any other described shape such as Voronoi cells (Chen *et al*. 2011, Amani *et al*. 2014) have been presented. Selective placement of nodes helps in reducing interpolation error whereas refinement of integration cells (Joldes *et al*. 2015) eliminates integration errors. Hence this needs serious consideration in formulation and solution.

This paper presents the refinement of nodal densities based on strain energy in an environment of EFG based MeshFree method. EFG Method is formulated for a 2D modelling of plate structures. Two popular flat plate problems with high stress gradients are considered to demonstrate the refinement scheme. One is by introducing symmetrical semi-circular notches at the top and bottom of the plate and the other by introducing a line crack under mode I and mode II fracture loading. Both the problems highlight the computational efficacy of the developed strain based adaptive refinement technique in the reduction of number of nodes and cells.

2. Mathematical formulation

Mathematical formulations of exponential weighting function, EFG method, Stress intensity computation by energy release rate, crack propagation angle and the methodology of crack propagation are discussed in the sections followed.

2.1 Shape function by Moving Least Square (MLS) technique

The exponential weighting function has been adopted for the construction of MLS shape function. The weighting function defined for a 2D space in $\xi\eta$ coordinates is written as

$$W(\xi - \xi_I, \eta - \eta_I) = W_1(\xi - \xi_I)W_2(\eta - \eta_I) = e^{-\left(\frac{d_\xi}{\alpha}\right)^2} e^{-\left(\frac{d_\eta}{\alpha}\right)^2} \tag{1}$$

where d_ξ and d_η can be written as $d_\xi = {|\xi - \xi_I|} / {d_{w\xi}}$ and $d_\eta = {|\eta - \eta_I|} / {d_{w\eta}}$ respectively. (ξ, η) is any point in the domain, (ξ_I, η_I) is the point/node whose weight is computed, $d_{w\xi}$ and $d_{w\eta}$ are the smoothing lengths of the domain in the directions and (ξ, η) are the natural coordinates that are defined for integration cells and the stiffness matrix is formulated in this coordinate system.

The shortest distances between the point-of-interest and the node has been computed using diffraction method as discussed by Liu (2009). Shape function or interpolation of field variables decides the accuracy of the results obtained in any numerical method. $u(\xi, \eta)$ are the functions of field variable defined in the 2D domain and its approximation at any point is given as

$$u(\xi, \eta) = \sum_{I=1}^{n} N_I u_I = \sum_{I=1}^{n} p^T A^{-1} B_I u_I \tag{2}$$

where, $\quad A(\xi, \eta) = \sum_{I=1}^{n} W(\xi - \xi_I, \eta - \eta_I) p^T(\xi_I, \eta_I) p(\xi_I, \eta_I) \quad$ and $\quad B_I = W(\xi - \xi_I, \eta - \eta_I) p(\xi_I, \eta_I) \quad$,

$p^T(\xi, \eta) = \{1, \xi, \eta, \xi\eta, \xi^2, \eta^2, \xi^2\eta, \xi\eta^2, \xi^2\eta^2, \ldots\ldots m\}$, u_I is the field variable and n is the number of nodes chosen for the construction of shape function at the point-of-interest.

2.2 Plate formulation

The kinematic relation for the 2D plate based on the coordinate systems shown in Fig. 1 can written as

$$\left. \begin{aligned} u &= u_0 + z\theta_y \\ v &= v_0 - z\theta_x \\ w &= w_0 \end{aligned} \right\} \tag{3}$$

where, u_0, v_0 and w_0 are mid-plane displacements of the plate along x, y and z axis, respectively and θ_x, θ_y are the mid-plane rotations along x, y axis, respectively (Refer Fig. 1).

On the basis of Eqs. (2) and (3), the strain-displacement relation may be written in the form

$$\begin{Bmatrix} \varepsilon_{xx}^0 \\ \varepsilon_{yy}^0 \\ \gamma_{xy}^0 \\ \kappa_x \\ \kappa_y \\ \kappa_{xy} \\ \gamma_{yz} \\ \gamma_{xz} \end{Bmatrix} = \sum_{I=1}^{n} [B_I] \begin{Bmatrix} u_{0I} \\ v_{0I} \\ w_{0I} \\ \theta_{xI} \\ \theta_{yI} \end{Bmatrix} = \sum_{I=1}^{n} \begin{bmatrix} \frac{\partial N_I}{\partial x} & 0 & 0 & 0 & 0 \\ 0 & \frac{\partial N_I}{\partial y} & 0 & 0 & 0 \\ \frac{\partial N_I}{\partial y} & \frac{\partial N_I}{\partial x} & 0 & 0 & 0 \\ 0 & 0 & 0 & 0 & \frac{\partial N_I}{\partial x} \\ 0 & 0 & 0 & -\frac{\partial N_I}{\partial y} & 0 \\ 0 & 0 & 0 & -\frac{\partial N_I}{\partial x} & \frac{\partial N_I}{\partial y} \\ 0 & 0 & \frac{\partial N_I}{\partial y} & 0 & -N_I \\ 0 & 0 & \frac{\partial N_I}{\partial x} & N_I & 0 \end{bmatrix} \begin{Bmatrix} u_{0I} \\ v_{0I} \\ w_{0I} \\ \theta_{xI} \\ \theta_{yI} \end{Bmatrix} \tag{4}$$
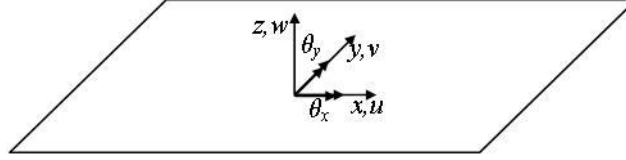
Fig. 1 Displacements and rotations about the mid-surface in plate formulation

where, $\varepsilon_{xx}^0 = \frac{\partial u_0}{\partial x}$ and $\varepsilon_{yy}^0 = \frac{\partial v_0}{\partial y}$ are the in-plane normal strains; $\gamma_{xy}^0 = \frac{\partial u_0}{\partial y} + \frac{\partial v_0}{\partial x}$ is the in-plane

shear strain; $\kappa_x = \frac{\partial \theta_y}{\partial x}$, $\kappa_y = -\frac{\partial \theta_x}{\partial y}$ and $\kappa_{xy} = \frac{\partial \theta_y}{\partial y} - \frac{\partial \theta_x}{\partial x}$ are the curvature strains of the mid-surface

of the plate, n is the number of nodes participating the construction of shape function and B is the strain-displacement matrix.

The stress-strain relation in terms of forces, moments, strains and curvatures about the mid-surface as shown in Fig. 1, is represented in the form

$$\begin{Bmatrix} N_x \\ N_y \\ N_{xy} \\ M_x \\ M_y \\ M_{xy} \\ Q_x \\ Q_y \end{Bmatrix} = \overbrace{\begin{bmatrix} \bar{C}_{11}h & \bar{C}_{12}h & 0 & 0 & 0 & 0 & 0 & 0 \\ \bar{C}_{12}h & \bar{C}_{11}h & 0 & 0 & 0 & 0 & 0 & 0 \\ 0 & 0 & \bar{C}_{66}h & 0 & 0 & 0 & 0 & 0 \\ 0 & 0 & 0 & \bar{C}_{11}\frac{h^3}{12} & \bar{C}_{12}\frac{h^3}{12} & 0 & 0 & 0 \\ 0 & 0 & 0 & \bar{C}_{11}\frac{h^3}{12} & \bar{C}_{22}\frac{h^3}{12} & 0 & 0 & 0 \\ 0 & 0 & 0 & 0 & 0 & \bar{C}_{66}\frac{h^3}{12} & 0 & 0 \\ 0 & 0 & 0 & 0 & 0 & 0 & \bar{C}_{44}h & 0 \\ 0 & 0 & 0 & 0 & 0 & 0 & 0 & \bar{C}_{55}h \end{bmatrix}}^{[MAT]} \begin{Bmatrix} \varepsilon_{xx}^0 \\ \varepsilon_{yy}^0 \\ \gamma_{xy}^0 \\ \kappa_x \\ \kappa_y \\ \kappa_{xy} \\ \gamma_{yz} \\ \gamma_{xz} \end{Bmatrix} \quad (5)$$

where, N_x, N_y and N_{xy} are the forces, M_x, M_y and M_{xy} are the moments, Q_x and Q_y are the shear forces, h is the thickness of the plate, $\bar{C}_{11} = \frac{E}{1-v^2}$, $\bar{C}_{12} = \frac{vE}{1-v^2}$, $\bar{C}_{44} = \bar{C}_{55} = \bar{C}_{66} = \frac{E}{2(1+v)}$, E is the

Youngs modulus of the material, v is the Poisson ratio.

Gauss quadrature for numerical integration is carried out using background cells, which are square in shape covering entire problem space without overlaps. Using Eqs. (4) and (5), the stiffness matrix representation in natural co-ordinates can be written as in Eq. (6)

$$K = \sum_{i=1}^{m_g} \sum_{j=1}^{n_g} w_i w_j B^T\left(\xi_i, \eta_j\right)[Mat]B\left(\xi_i, \eta_j\right)\left|J\left(\xi_i, \eta_j\right)\right| \quad (6)$$

where, $J = \begin{bmatrix} \sum_{I=1}^{n} \frac{\partial N_I}{\partial \xi} x_I & \sum_{I=1}^{n} \frac{\partial N_I}{\partial \xi} y_I \\ \sum_{I=1}^{n} \frac{\partial N_I}{\partial \eta} x_I & \sum_{I=1}^{n} \frac{\partial N_I}{\partial \eta} y_I \end{bmatrix}$ and x_I *and* y_I are the coordinates of the nodes in the domain for

construction of shape function, where, m_g and n_g are the number of Gauss points along x and y coordinates.

2.3 Application of displacement constraints and loads

MLS based MeshFree method employs Lagrange multipliers for imposition of boundary condition, as the method does not satisfy Kronecker delta property. Displacement constraints are defined where the boundary condition is to be imposed. If Γ_λ is the 1D (one dimensional) domain along which the boundary displacement is to be made zero, then the Lagrange multiplier matrix G may be written as

$$G = -\int_{\Gamma_\lambda} N_\lambda^T N d\Gamma_\lambda = -\sum_{i=1}^{n_\lambda} w_i N_\lambda^T(\xi_i) N(\xi_i) \frac{L_\lambda}{2} \tag{7}$$

where, N_λ is the shape function that interpolates λ along the domain Γ_λ, L_λ is the length of the domain and n_λ is the number of Gauss points along the domain Γ_λ required for numerical integration and ξ is the natural coordinate in 1D that defines the boundary domain.

And the Lagrange multiplier matrix G imposes the required boundary constraints as follows

$$\begin{bmatrix} K & G^T \\ G & 0 \end{bmatrix} \begin{Bmatrix} u \\ \lambda \end{Bmatrix} = \begin{Bmatrix} F \\ 0 \end{Bmatrix} \tag{8}$$

where λ is the Lagrange multiplier, and F is applied force.

If Γ_p is the 1D domain along which the uniform pressure load is to be applied and it can be represented as shown

$$f = p \int_{\Gamma_p} N \, d\Gamma_p = p \sum_{i=1}^{n_p} w_i \, N(\xi_i) \frac{L_p}{2} \tag{9}$$

where p is the applied pressure along the domain Γ_p, L_p is the length domain Γ_p and n_p is the number of Gauss points along the domain Γ_p.

2.4 Stress computation schemes

The displacements u is obtained by solving the Eq. (8) and is substituted in Eq. (10) which yields stresses

$$\sigma = \bar{C} Z B u \tag{10}$$

where,

$$\bar{C} = \begin{bmatrix} \bar{C}_{11} & \bar{C}_{12} & 0 & 0 & 0 \\ \bar{C}_{12} & \bar{C}_{11} & 0 & 0 & 0 \\ 0 & 0 & \bar{C}_{44} & 0 & 0 \\ 0 & 0 & 0 & \bar{C}_{55} & 0 \\ 0 & 0 & 0 & 0 & \bar{C}_{66} \end{bmatrix}, \quad Z = \begin{bmatrix} 1 & 0 & 0 & z & 0 & 0 & 0 & 0 \\ 0 & 1 & 0 & 0 & z & 0 & 0 & 0 \\ 0 & 0 & 1 & 0 & 0 & z & 0 & 0 \\ 0 & 0 & 0 & 0 & 0 & 0 & 1 & 0 \\ 0 & 0 & 0 & 0 & 0 & 0 & 0 & 1 \end{bmatrix}$$ and z is the coordinate in
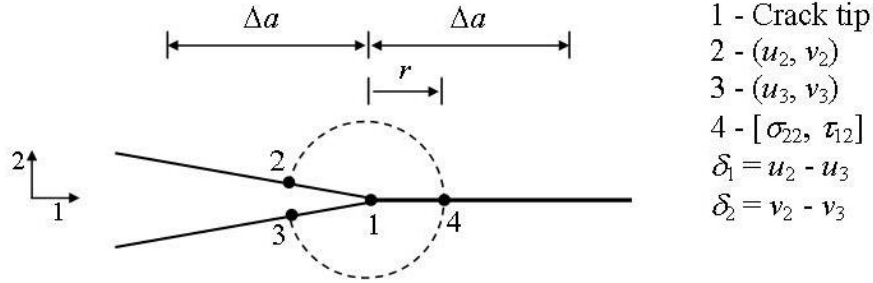
Fig. 2 Crack tip

thickness direction of the plate and varies from $-h/2$ to $h/2$

From these stresses the principal and von Mises stresses are calculated in Eqs. (11) and (12) respectively.

$$\sigma_{1,2} = \frac{\sigma_{xx}+\sigma_{yy}}{2} \pm \sqrt{\left(\frac{\sigma_{xx}-\sigma_{yy}}{2}\right)^2 + \tau_{xy}^2} \tag{11}$$

$$\sigma_v = \sqrt{\sigma_1^2 - \sigma_1\sigma_2 + \sigma_2^2} \tag{12}$$

3. Methodology for crack propagation and adaptive refinement

3.1 Tracing crack propagation with SIF as basis

The stress intensity factor can be computed from the energy release rate, which at the crack tip as shown in Fig. 2 can be written as

$$G_I = \frac{1}{2\Delta a}\int_0^{\Delta a} \sigma_{22}(r)\delta_2(\Delta a - r)dr = \frac{1}{4}\sum_{i=1}^{n_c} w_i\sigma_{22}(\xi)\delta_2(1-\xi) \tag{13}$$

$$G_{II} = \frac{1}{2\Delta a}\int_0^{\Delta a} \sigma_{12}(r)\delta_1(\Delta a - r)dr = \frac{1}{4}\sum_{i=1}^{n_c} w_i\tau_{12}(\xi)\delta_1(1-\xi) \tag{14}$$

where Δa is the assumed incremental length of the crack behind the crack tip, r is the length that varies from 0 to Δa and n_c is the number of Gauss points used along the length Δa, δ_1 and δ_2 is the amount by which the crack opens on application of load and is measured behind the crack tip at r along the local axis 1 and 2, respectively, σ_{22} and τ_{12} are the normal and shear stresses measured ahead of the crack tip at r in the local axis (123).

For any inclined crack the global stresses and displacements are transformed to the local axis, where the local axis is defined by the crack as shown in Fig. 2.

From Eqs. (13) and (14), the stress intensity factors are written as

$$K_I = \sqrt{G_I E} \quad and \quad K_{II} = \sqrt{G_{II} E} \tag{15}$$

For the crack subjected to mode I and II loading, the possibility of propagation is determined by critical SIF as in Eq. (16).

$$\frac{4\sqrt{2}K_{II}^{3}\left(K_{I}+3\sqrt{K_{I}^{2}+8K_{II}^{2}}\right)}{\left(K_{I}^{2}+12K_{II}^{2}-K_{I}\sqrt{K_{I}^{2}+8K_{II}^{2}}\right)^{3/2}}\geq K_{Ic} \tag{16}$$

where K_{Ic} is the critical stress intensity factor of the material. If K_{Ic} is greater than or equal to 4427 N/mm^2 for the material considered in this investigation (mild steel) then the crack grows.

The direction of crack propagation is given by θ_c in Eq. (17)

$$\theta_{c}=2\tan^{-1}\left(\frac{1}{4}\left(\frac{K_{I}}{K_{II}}\pm\sqrt{\left(\frac{K_{I}}{K_{II}}\right)^{2}+8}\right)\right) \tag{17}$$

3.2 Strain energy based adaptive refinement

Adaptive refinement requires the refinement of both integration cells and nodes in the problem domain. The refinement of integration cell reduces the integration error and the refinement of nodes reduces the polynomial error. Determination of strain energy densities and identification of areas contributing to it and adoption of cell and node refinement to facilitate reduction of errors and faster convergence is formulated as explained below.

3.2.1 Strain energy density in integration cell and triangular cell

The strain energy density in integration cell is computed for the ith cell as

$$S_{IC}^{(i)}=\frac{\frac{1}{2}\int_{v_{c}^{(i)}}\sigma^{T}\varepsilon\,dV_{c}^{(i)}}{\int_{v_{c}^{(i)}}dV_{c}^{(i)}}=\frac{t\sum_{j=1}^{n}w_{j}\sigma^{T}\left(\xi_{j},\eta_{j}\right)\varepsilon\left(\xi_{j},\eta_{j}\right)\left|J\left(\xi_{j},\eta_{j}\right)\right|}{t\sum_{j=1}^{n}w_{j}\left|J\left(\xi_{j},\eta_{j}\right)\right|} \tag{18}$$

where V_c is the volume of the ith cell; σ and ε are the stresses and strains; n is the number of Gauss points in the integration cell, w_j is the Gauss weight

Then the strain energy density in the triangular cell is computed from the contributions of strain energy from the integration cells based on the area contributed from each of these cells. This is mathematically represented for the ith triangular cell as

$$S_{TC}^{(i)}=\frac{\sum_{j=1}^{n}S_{IC}^{(j)}\bar{A}_{TC}^{(j)}}{A_{TC}^{(i)}} \tag{19}$$

where n is the number of integration cells that overlaps a given i^{th} triangular cell; $\bar{A}_{TC}$ is the area common to the jth integration cell and the ith triangular cell, $A_{TC}^{(i)}$ is the area of the ith triangular cell.

3.2.2 Cell refinement

In cell refinement, the cell with high strain energy density above the set threshold value ($\bar{S}_{IC}$) is chosen and refined by dividing one cell into four cells (Fig. 3). The process is continued till the energy density in all the cells is below the set threshold value ($\bar{S}_{IC}$).
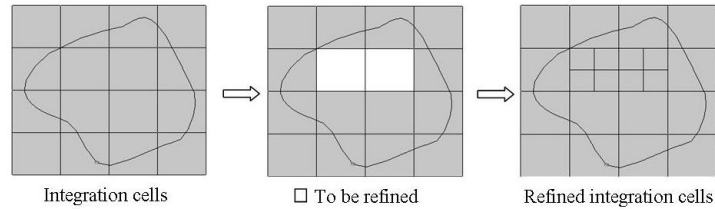
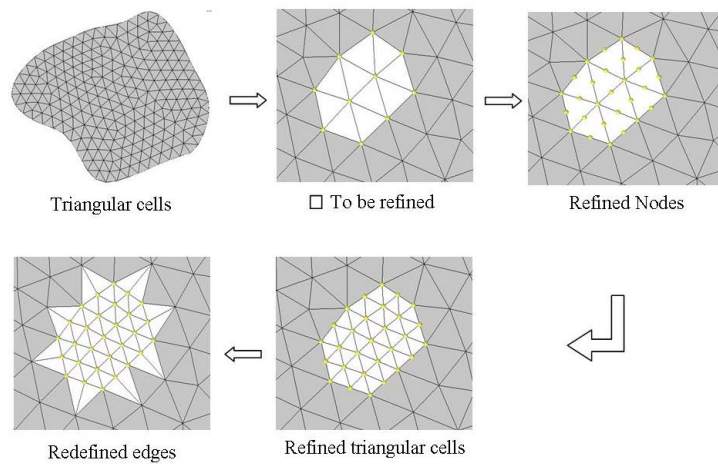Fig. 3 Refinement of integration cells by sub-dividing each cell into four cells

Fig. 4 Refinement of nodes by sub-dividing each triangular cell into four cells

3.2.3 Node refinement

The nodal refinement is achieved in the following three steps:

1. The triangular cells with high strain energy densities above the set threshold value ($\bar{S}_{TC}$) are identified for refinement

2. Each of these identified triangular cells are subdivided into four triangular cells thus adding additional nodes on the vertices of the triangle in the region of refinement.

3. Further, the triangular cells are redefined such that no free edges exist in the refined region.

The detailed steps of nodal refinement are shown in Fig. 4.

The threshold is taken in this work as the convergence of the of the stress value, i.e., if the stresses from the previous iteration do not have more than 10% difference then the further refinement is stopped. The percentage difference can vary depending on the level of accuracy required. The procedure discussed in represented in the form of flow chart in Fig. 5.

4. Results and discussion

The developed formulation of EFG based MeshFree method (Sec. 2) and the methodology for crack propagation and adaptive refinement (Sec. 3) are coded in MATLAB®. The numerical studies are carried using standard benchmark problems and are discussed in this section.

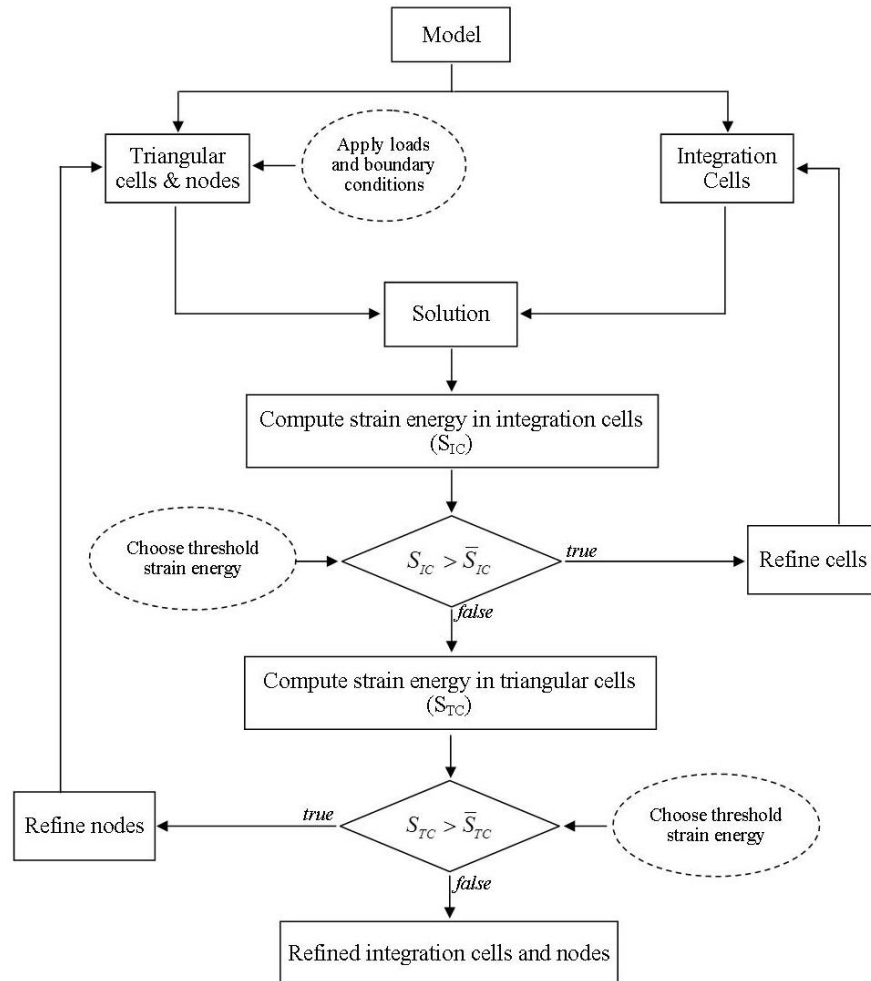Verification of MeshFree method using a 2D rectangular beam subjected to axial load and

Fig. 5 Methodology for adaptive refinement of integration cells and nodal density

computation of SIF using a rectangular plate with vertical crack at the centre is presented. Further two benchmark cases that highlight the efficacy of the adaptive refinement scheme have been detailed. The same nodal locations have been employed in both FEM and MeshFree solutions to make comparison more meaningful and highlight the efficacy of MeshFree method. For all the cases material properties have been taken as, modulus of elasticity E=210 GPa, Poisson ratio v=0.33 and plate thickness h=2 mm. The results of the studies have been presented, compared, verified, validated, discriminated and efficacy of EFG method has been highlighted.

4.1 Validation of developed procedures

4.1.1 2D rectangular beam subjected to axial load

To verify the MeshFree procedure, a simple 2D rectangular beam is considered (Fig. 6) for the study. One end of the beam is constrained and the other end is axially loaded with uniformly distributed load as shown in Fig. 6.
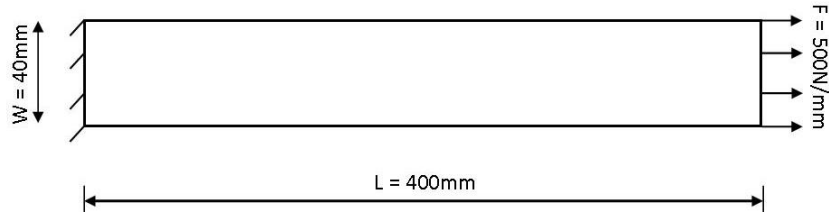
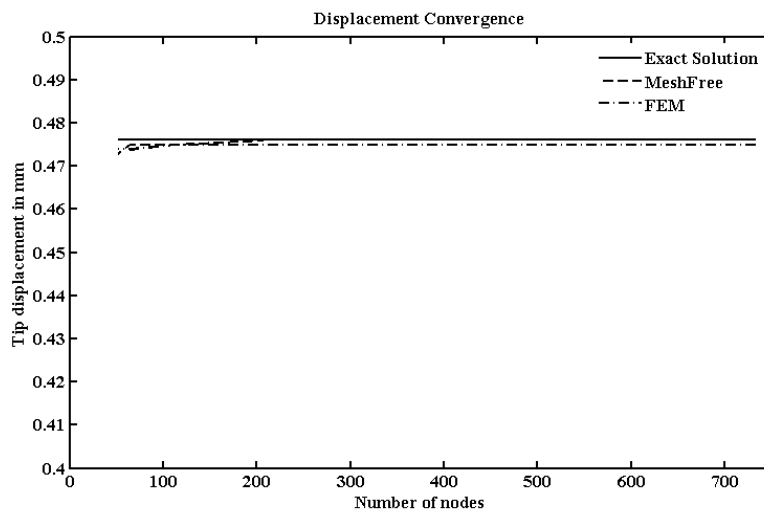Fig. 6 A simple 2D rectangular beam structure

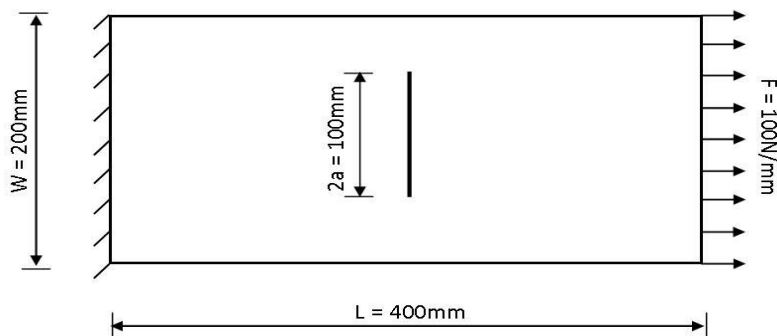Fig. 7 Displacement convergence in 2D rectangular beam structure

Fig. 8 Geometrical configuration of plate with centre crack

Convergence study has been carried out by incrementally increasing the number of nodes from 63 to 700. Fig. 7 shows convergence rates of EFG method having better accuracy level faster than FEM. Usually axially loaded cases are known to converge faster with less nodes than transversely loaded cases.

4.1.2 Rectangular plate with vertical crack

Crack path is directed by the SIF, when the SIF in the component crosses the threshold SIF

Table 1 Computed results for plate with centre crack

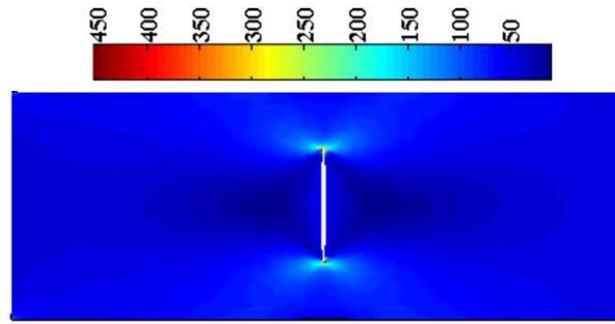| Displacement (mm)	Stress (N/mm^2)	SIF (N/mm$^{3/2}$)	
		Closed-form	MFree
0.119	516.31	680	673

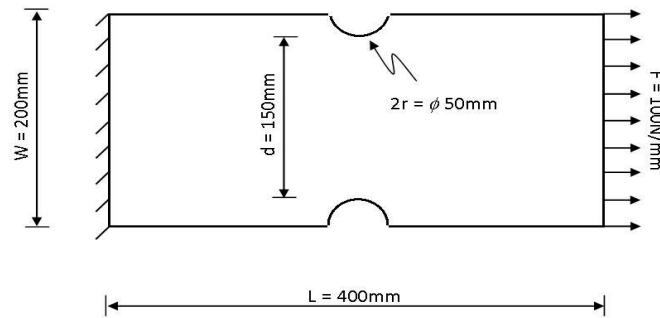Fig. 9 Von Mises stress distribution in a rectangular plate with central vertical crack

Fig. 10 The geometry of high stress gradient plate

(Eq. (16)) the crack starts to propagate. In this section SIF computed by MeshFree is verified with the closed-form solution using a standard problem in Fig. 8. The SIF is computed under uniformly distributed axial load using the energy release approach (Eqs. (13)-(15)). One end of the rectangular plate is constrained and the other end is axially loaded with uniformly distributed load as shown in Fig. 8. A vertical crack is introduced at the centre of the plate and at one of the crack tips, the energy release rate and thereby the SIF is computed.

The closed-form solution for the case stated in Fig. 8 is readily available in literature and the present solution using MeshFree compares well with the same as tabulated (Table 1). Fig. 9 shows the distribution of von Mises stress. This exercise thus validates the procedure of computing the SIF of a given crack geometry.

4.2 Benchmark problem 1-rectangular plate with two semi-circular notches

4.2.1 Problem description

Plate with two semi-circular notches (Fig. 10) is a classic example of a plate with high stress concentration. Fig. 10 shows the configuration of the plate considered, with left end of the plate

Table 2 Displacement, stress and SCF for plate with semi-circular notch

Nodal density	Max. Displacement (mm)		Maximum Stress σ_{xx} (N/mm^2)		Stress Concentration Factor (SCF)		
	FEM	MFree	FEM	MFree	Exact	FEM	MFree
Coarse	0.100	0.102	89.18	124.65	2.26	1.33	1.87
Fine	0.101	0.102	134.3	148.01	2.26	2.01	2.22
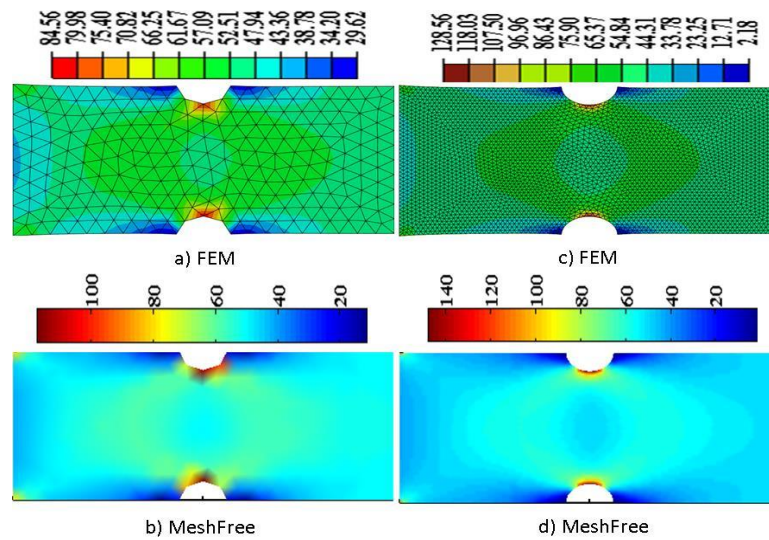
Fig. 11 Von-Mises stress plot in rectangular plate with two semi-circular notches

constrained and in the right end has the uniformly distributed load in axial direction. Table 2 shows the comparison of displacement, stress and their validation with SCF, where the plate was analysed with coarse and fine nodal densities, i.e., by having 250 nodes and 3500 nodes, respectively. MeshFree shows better approximation both in terms of displacement and stress compared to that of FEM. For the given plate MeshFree method has 2% error compared to 11% in FEM in the case of fine nodal density. Smoother stress distribution can be observed in MeshFree method (Fig. 11) for both coarse and fine nodal densities.

4.2.2 Adaptive refinement

The strategy for adaptive refinement is detailed in this section. In the first iteration, the displacements and stresses are computed with very coarse density of nodes and integration cells (Table 3). In each iteration, the cells that lie in the top 20% of the strain energy levels are subjected to refinement. Table 3 shows the refinement iterations followed and the number of nodes and cells obtained in each step.

In Figs. 12 and 13, the strain energy distribution of integration and triangular cells are shown, respectively. It can be observed that the refinement of the integration and triangular cells occurring at each step of the iteration is concentrated around the high stress regions. As the iterations increase, the computed stress values saturate and the refinement is stopped when the computed stress difference is less than 10%. A drastic reduction of about 86% of nodes with acceptable
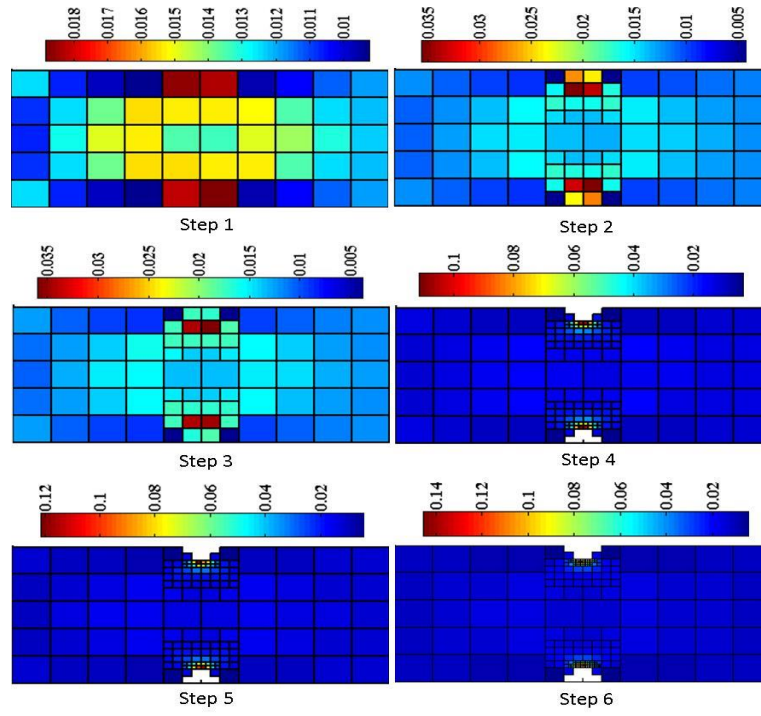
Fig. 12 Strain energy distribution in integration cells of plate with semi-circular notches
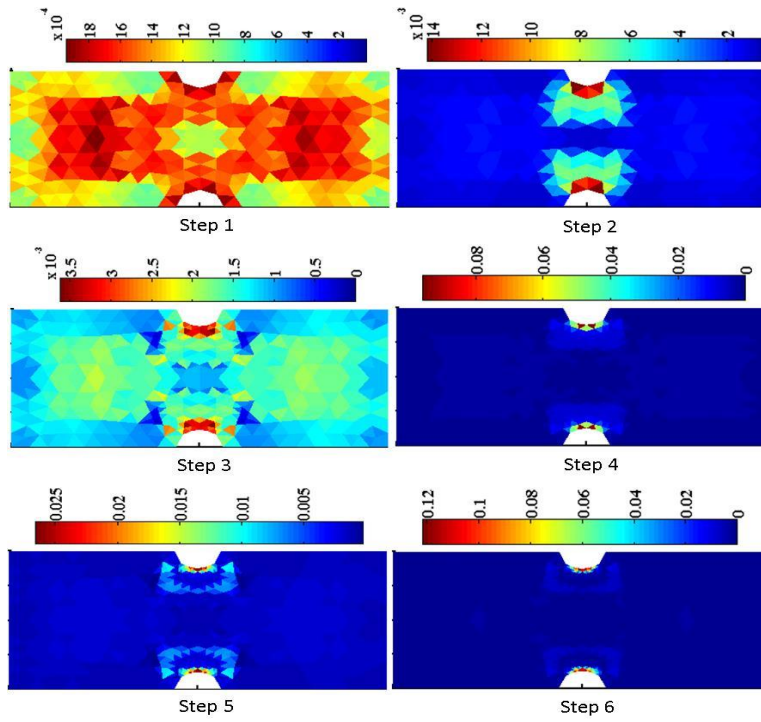
Fig. 13 Strain energy distribution in triangular cells of plate with semi-circular notches
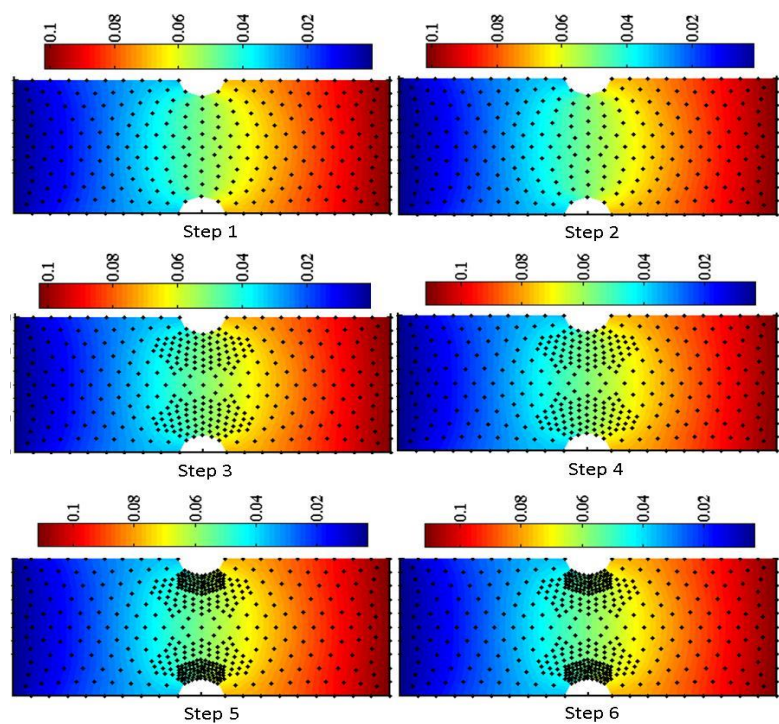
Fig. 14 Displacement plot of adaptively refined plate with semi-circular notches
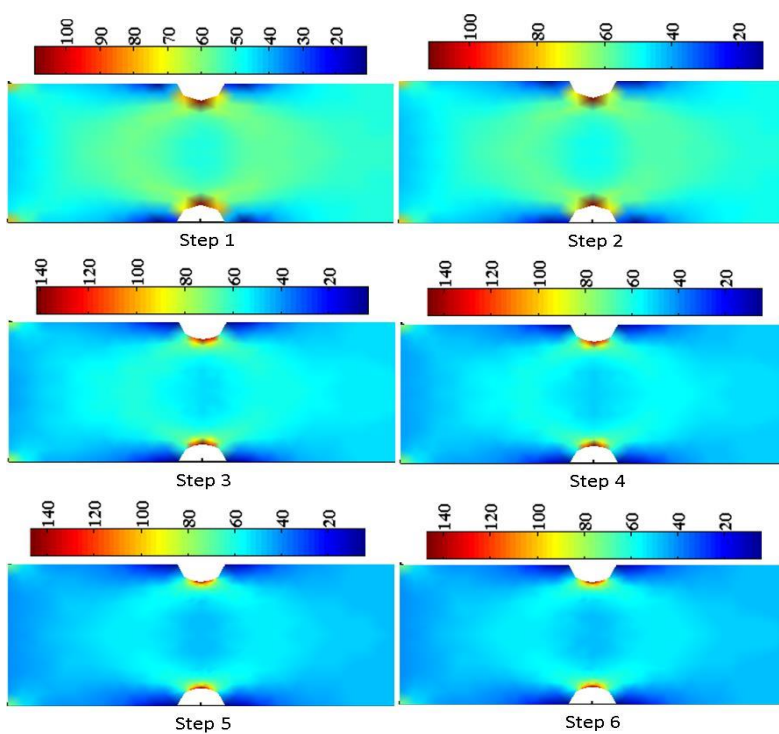
Fig. 15 Von Mises stress plot of adaptively refined plate with semi-circular notches

Table 3 Adaptive refinement iterations in plate with semi-circular notches

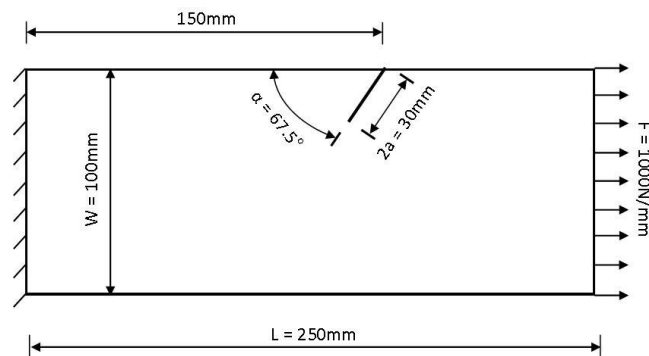| Refinement of	No. of Cells	No. of Nodes	Displacement (mm)	Stress (N/mm^2)
None	50	261	0.101	116.86
Cell	74	261	0.101	120.14
Node	74	367	0.102	151.1
Cell	146	367	0.102	157.51
Node	146	485	0.102	164.8
Fine nodal density	200	3580	0.102	148.01

Fig. 16 Problem description for plate with inclined crack

accuracy has been observed. Displacement distribution along with the refined nodes and von Mises stress distributions are shown in Figs. 14 and 15 respectively.

4.3 Benchmark problem 2-rectangular plate with angled edge crack

4.3.1 Problem description

The angled edge crack in a rectangular plate is a crack propagation problem discussed by Patricio and Mattheij (2007), where the crack propagation has been simulated using XFEM and validated experimentally. The geometrical configuration of the plate is shown in Fig. 16, where the crack is angled at 67.5 deg. to the longer edge of the plate, one of the shorter edges is fixed and on the other uniformly distributed load is applied.

The accurate crack path can be traced with fine distribution of nodes at least around the region of the crack (addressed in adaptive refinement). Step length i.e., the assumed length of crack that propagates after each stage should be smaller for better approximation. The nodes have been distributed uniformly (fine) in the entire plate and a step length of 7.5mm has been taken.

The critical SIF value of steel is 4427 N/mm^2 and under the applied load shown in Fig. 16, the SIF value is greater than critical SIF value and is seen to increase as the crack grows (Table 4). Even after 5th iteration the crack continues to grow further and SIF continues to be above critical value and the angle at 0 deg. until the crack reaches the longer edge of the plate. The von Mises stress distribution of the crack at different iteration steps can be seen in Fig. 17 and the SIF values are shown in Table 4. The crack path traced matches well with the one presented by Patricio and Mattheij (2007).

Table 4 Displacement, stress and SCF for plate with inclined edge crack

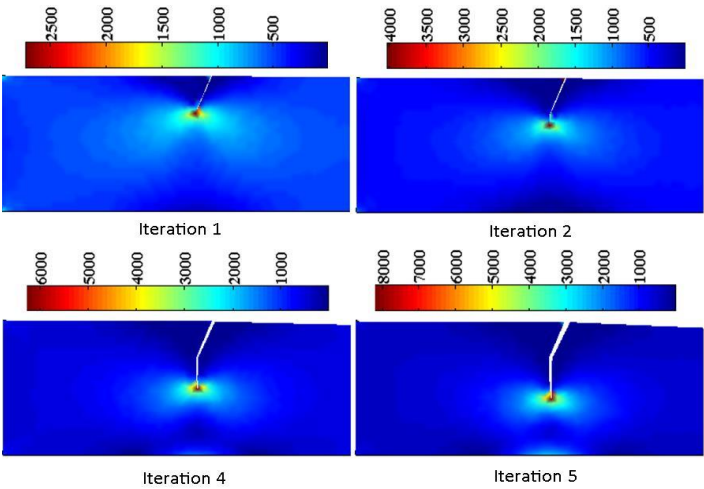| Iteration No.	Displacement (mm)	Stress (N/mm^2)	SIF (N/mm^2)	Remarks
1	0.938	2972.6	5373	propagates at 21.56^o
2	1.241	3820.5	7379	propagates at 0°
3	1.795	5817.1	10727	propagates at 0°
4	2.795	7753.7	14527	propagates at 0°
5	4.341	10094	19714	continues at 0° till breakage

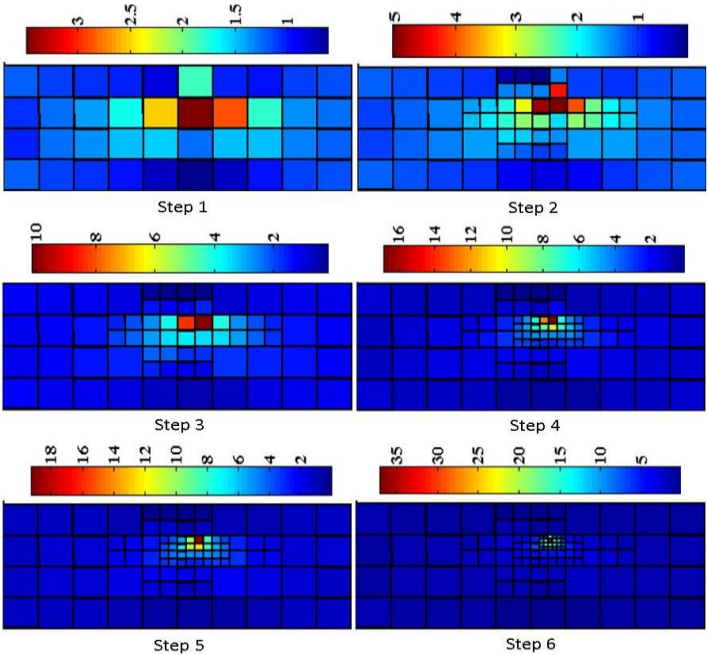Fig. 17 Von Mises stress plot for plate with inclined edged crack

Fig. 18 Strain energy distribution in integration cells for plate with inclined edge crack
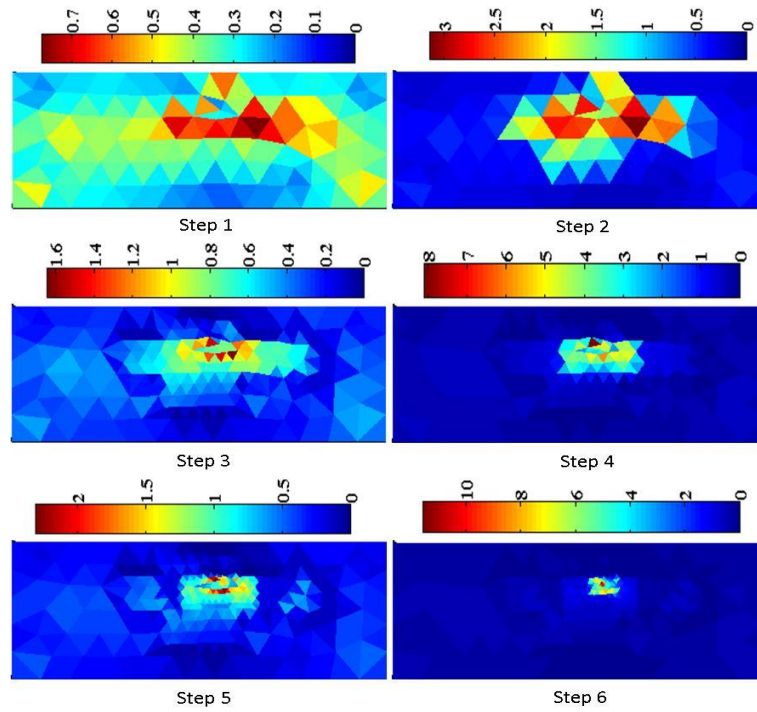
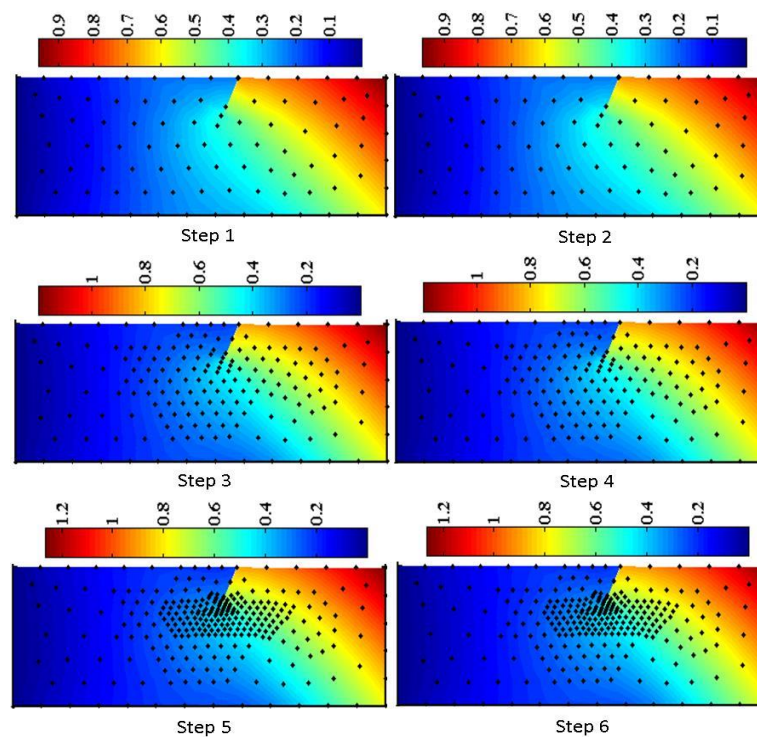Fig. 19 Strain energy distribution in triangular cells for plate with inclined edge crack

Fig. 20 Displacement plot of adaptively refined plate with inclined edge crack
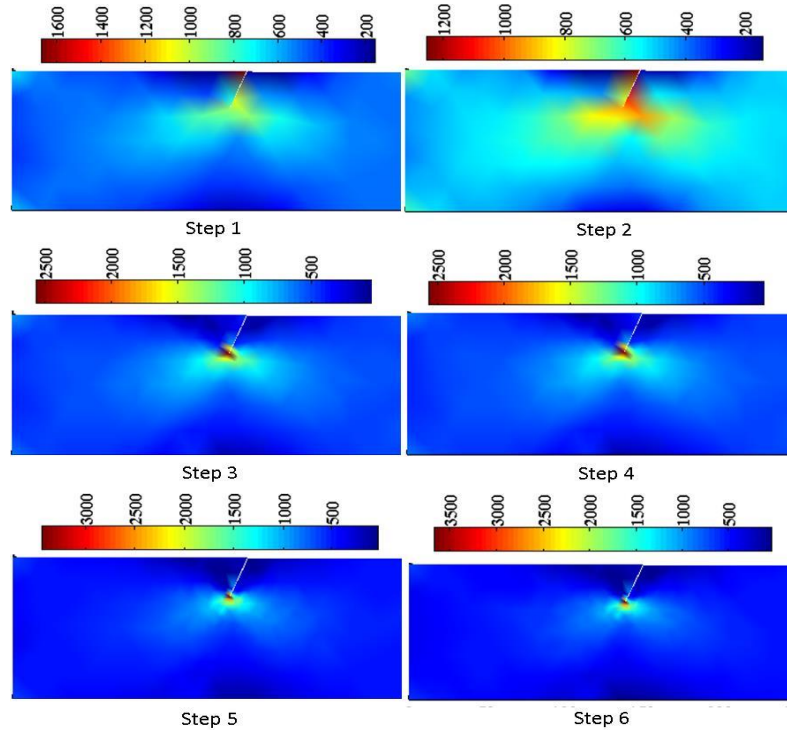
Fig. 21 Von Mises stress plot of adaptively refined plate with inclined edge crack

Table 5 Adaptive refinement iterations in plate with inclined edge crack

Refinement of	No. of Cells	No. of Nodes	Displacement (mm)	Stress (N/mm^2)
None	40	96	0.852	1036.8
Cell	67	96	0.853	1036.5
Node	67	183	0.994	2874.5
Cell	91	183	0.995	2886.8
Node	91	291	1.03	2978.8
fine nodal density	208	1211	0.938	2972.6

4.3.2 Adaptive refinement

The displacements and stresses computed for very coarse density of nodes and integration cells (Table 5) in the initial iteration. Followed by the refinement of top 20% of the strain energy levels has been carried out. Refinement iterations and the number of nodes and cells obtained in each step is tabulated in Table 5.

The refinement of integration and triangular cells around the crack tip occurs after each iteration and the strain energy distribution for the same can be observed in Figs. 18 and 19. About 75% reduction of nodes can be observed with acceptable accuracy. Further Displacement distributions along with the refined nodes (Fig. 20) and von Mises stress distributions (Fig. 21) are presented.

5. Conclusions

The efficacies of EFG method based adaptive refinement in addressing stress concentration effects have been demonstrated. The adaptive refinement strategies proposed and formulated have yielded encouraging results by way of reduction in number of nodes required to accomplish acceptable convergence rates and limits. About 86% and 76% reduction in nodes requirement have been accomplished for stress concentration and crack propagation problems respectively. The formulation finds potential as a decision making tool in real-time health monitoring of structures.

Acknowledgements

References

Amani, J., Saboor Bagherzadeh, A. and Rabczuk, T. (2014), "Error estimate and adaptive refinement in mixed discrete least squares meshless method", *Math. Prob. Eng.*, Article ID 721240, 16

Belytschko, T., Lu, Y.Y. and Gu, L. (1995), "Crack propagation by element-free Galerkin methods", *Eng. Fract. Mech.*, **51**(2), 295-315.

Belytschko, T. and Black, T. (1999), "Elastic crack growth in finite elements with minimal remeshing", *Int. J. Numer. Methd. Eng.*, **45**(5), 601-620.

Bordas, S., Rabczuk, T. and Zi, G. (2008), "Three-dimensional crack initiation, propagation, branching and junction in non-linear materials by an extended meshfree method without asymptotic enrichment", *Eng. Fract. Mech.*, **75**(5), 943-960.

Bouchard, P.O., Bay, F. and Chastel, Y. (2003), "Numerical modelling of crack propagation: automatic remeshing and comparison of different criteria", *Comp. Methd. Appl. Mech. Eng.*, **192**(35), 3887-3908.

Chen, L., Zhang, G.Y., Zhang, J., Nguyen-Thoi, T. and Tang, Q. (2011), "An adaptive edge-based smoothed point interpolation method for mechanics problems", *Int. J. Comput. Math.*, **88**(11), 2379-2402.

Chow, W.T. and Atluri, S.N. (1995), "Finite element calculation of stress intensity factors for interfacial crack using virtual crack closure integral", *Comput. Mech.*, **16**(6), 417-425.

Dolbow, J., Moës, N. and Belytschko, T. (2000), "Discontinuous enrichment in finite elements with a partition of unity method", *Finite Elem. Anal. Des.*, **36**(3), 235-260.

Eigel, M., George, E. and Kirkilionis, M. (2010), "A mesh-free partition of unity method for diffusion equations on complex domains", *IMA J. Numer. Anal.*, **30**(3), 629-653.

Fleming, M., Chu, Y.A., Moran, B., Belytschko, T., Lu, Y.Y. and Gu, L. (1997), "Enriched element-free Galerkin methods for crack tip fields", *Int. J. Numer. Meth. Eng.*, **40**(8), 1483-1504

Giner, E., Sukumar, N., Tarancon, J.E. and Fuenmayor, F.J. (2009), "An Abaqus implementation of the extended finite element method", *Eng. Fract. Mech.*, **76**(3), 347-368.

Häussler-Combe, U. and Korn, C. (1998), "An adaptive approach with the element-free-Galerkin method", *Comput. Meth. Appl. Mech. Eng.*, **162**(1), 203-222.

Joldes, G.R., Wittek, A. and Miller, K. (2015), "Adaptive numerical integration in Element-Free Galerkin methods for elliptic boundary value problems", *Eng. Anal. Bound. Elem.*, **51**, 52-63.

Krysl, P. and Belytschko, T. (1999), "The Element Free Galerkin method for dynamic propagation of arbitrary 3D cracks", *Int. J. Numer. Meth. Eng.*, **44**(6), 767-800.

Liu, G.R. and Tu, Z.H. (2002), "An adaptive procedure based on background cells for meshless methods", *Comput. Meth. Appl. Mech. Eng.*, **191**(17), 1923-1943.

Liu, G.R. (2009), *Meshfree methods: moving beyond the finite element method*, Taylor & Francis.

Menouillard, T. and Belytschko, T. (2010), "Dynamic fracture with meshfree enriched XFEM", *Aata Mechanica*, **213**(1-2), 53-69.

Mergheim, J., Kuhl, E. and Steinmann, P. (2005), "A finite element method for the computational modelling of cohesive cracks", *Int. J. Numer. Meth. Eng.*, **63**(2), 276-289.

Pant, M., Singh, I.V. and Mishra, B.K. (2013), "A novel enrichment criterion for modeling kinked cracks using element free Galerkin method", *Int. J. Mech. Sci.*, **68**, 140-149.

Patrıcio, M. and Mattheij, R. (2007), *Crack propagation analysis*, CASA Report, 07-03

Rabczuk, T., Bordas, S. and Zi, G. (2007), "A three-dimensional meshfree method for continuous multiple-crack initiation, propagation and junction in statics and dynamics", *Comput. Mech.*, **40**(3), 473-495.

Rabczuk, T. and Zi, G. (2007), "A meshfree method based on the local partition of unity for cohesive cracks", *Comput. Mech.*, **39(6)**, 743-760.

Sukumar, N. and Belytschko, T. (2000), "Arbitrary branched and intersecting cracks with the extended finite element method", *Int. J. Numer. Meth. Eng.*, **48**, 1741-1760.

Sukumar, N., Moës, N., Moran, B. and Belytschko, T. (2000), "Extended finite element method for three-dimensional crack modeling", *Int. J. Numer. Meth. Eng.*, **48**(11), 1549-1570.

Ullah, Z. and Augarde, C.E. (2013), "Finite deformation elasto-plastic modelling using an adaptive meshless method", *Comput. Struct.*, **118**, 39-52.

Wu, Y., Magallanes, J.M., Choi, H.J. and Crawford, J.E. (2012), "Evolutionarily coupled finite-element mesh-free formulation for modeling concrete behaviors under blast and impact loadings", *J. Eng. Mech.*, **139**(4), 525-536.

Zi, G., Rabczuk, T. and Wall, W. (2007), "Extended meshfree methods without branch enrichment for cohesive cracks", *Comput. Mech.*, **40**(2), 367-382.

CC